RSC Advances

PAPER

View Article Online
View Journal | View Issue

Cite this: *RSC Adv.*, 2026, **16**, 4708

Revealing the influence of Cr and Al additions on the corrosion of carbon steel in a supercritical CO_2–SO_2 environment

Rongdie Zhu,[a] Jinyang Zhu,*[a] Hangrui Shi,[a] Lining Xu,*[b] Yunan Zhang,[a] Zhile Yang,[b] Yuanliang Liu[a] and Hangqi Li[a]

The formation mechanism of corrosion product films of X65 and 5Cr2Al steels in CO_2-saturated aqueous phase environments containing 100 ppm and 300 ppm SO_2 impurities was investigated. Under both conditions, the corrosion rate of X65 was approximately ten times that of 5Cr2Al, with the main reaction being the formation of $FeCO_3$. In the CO_2-100 ppm SO_2 system, the inner layer of 5Cr2Al formed $Cr(OH)_3$ and $Al(OH)_3$ layers, while the outer layer formed $FeCO_3$. When the SO_2 concentration increased to 300 ppm, Cr and Al reacted synergistically with SO_2, forming a double-layer structure with an inner layer composed of $Cr(OH)_3$ and $Al(OH)_3$ and an outer layer composed of dense elemental sulfur. This film layer structure exhibited excellent corrosion resistance. *In situ* electrochemical measurement results in supercritical CO_2 environments with 300 ppm SO_2 further reveal that corrosion is aggressive for X65. While a semi-passivation phenomenon occurred for 5Cr2Al steel. This study indicates that a dense S elemental film can form only when Cr and Al are present and the SO_2 concentration reaches 300 ppm. 5Cr2Al is a suitable material choice for the injection tube in a mixed CO_2–SO_2 environment.

Received 1st December 2025
Accepted 11th January 2026

DOI: 10.1039/d5ra09269h

rsc.li/rsc-advances

1. Introduction

CO_2 capture and storage (CCS) technology is designed to reduce CO_2 emissions by capturing CO_2 from existing combustion plants, transporting it *via* pipelines under a supercritical state, and ultimately injecting it into deep geological formations *via* an injection tube for long-term storage. There are successful application cases, such as the Sleipner project in Norway. It is recognized as the world's first commercial-scale carbon storage project, storing approximately one million tons of CO_2 annually. CCS technology was proposed by the United Nations Global Climate Change Conference. It has been recognized as a critical solution for controlling CO_2 emissions.[1] It is safe, economical and has good applicability. Pure CO_2 poses almost no corrosion threat to steels.[2] However, impurities are inevitably present in the captured CO_2 stream (such as SO_2, NO_2, O_2, H_2S, and H_2O).[3,4] These impurities can damage the structural integrity of pipeline and injection tube. Therefore, it is necessary to explore the role of individual impurities in pipeline corrosion and their specific corrosion mechanisms.

During the injection stage, CO_2 will be injected into deep underground long-term storage layers containing a large amount of chlorides, which are the most preferred storage sites for CO_2 sequestration.[5] Water and erosive ions create active environments for corrosion reactions. SO_2, as one of the most common and notorious impurity gases, when dissolved in water, will acidify formation water and cause severe corrosion damage to steels.[6–8] Sun *et al.*[9] demonstrated that in the CO_2–H_2O–SO_2 system, even a small amount of water could affect the SO_2 corrosion behavior. SO_2 deteriorated the water chemistry characteristics, making it highly acidic. The water content in the supercritical (SC) CO_2/H_2O/impurities system is far below its solubility limit. A small amount of SO_2 significantly increased the corrosion rate.[10] ISO standard and DYNAMIS project[11,12] recommend SO_2 should be limited to 100 ppm. It is necessary to study the corrosion behavior when 100 ppm is compared with a higher concentration of SO_2. Besides, most studies on the impact of impurities in CO_2 streams have focused on supercritical (SC) CO_2 gas phases containing a small amount of water.[13–16] Therefore, it is also necessary to study the effect of impurities on steel in deep saline water under a SC CO_2 environment.

It is estimated that 10 Gt per year of CO_2 will require transportation to geological storage sites by 2050. This scale of deployment would necessitate the construction of an extensive pipeline network, including either 3000 lines of 12-inch diameter or 1000 lines of 20-inch diameter. Carbon steel pipelines are widely considered the most cost-effective solution for large-scale CO_2 transportation.[17–19] However, the injection of CO_2 transported to geological storage sites into saline aquifers presents more risks, including potential geomechanical

[a]*National Center for Materials Service Safety, University of Science and Technology Beijing, Beijing 100083, PR China. E-mail: zhujinyang@ustb.edu.cn*
[b]*Institute for Advanced Materials and Technology, University of Science and Technology Beijing, Beijing 100083, PR China. E-mail: xulining@ustb.edu.cn*

impacts (*e.g.*, crustal movement, ground deformation) and substantial liquid. As indicated in Table 1, conventional pipeline steels such as grades X65, N80, and P110 exhibit corrosion rates reaching up to 10 mm per year in aqueous phases. Consequently, standard carbon steels are demonstrably inadequate for meeting the operational requirements of such environments. Using corrosion-resistant alloys (CRAs), such as chromium-containing steels, is a promising method for effective corrosion control.[20] Under the same high-temperature and high-pressure conditions, using this type of steel can relatively reduce the wall thickness and provide cost savings. Furthermore, these materials also offer stronger collapse resistance and corrosion resistance compared to conventional carbon steels.[21] 13Cr has the lowest corrosion rate in the liquid phase (Table 1), but it is expensive and has a high investment cost. Extensive research has consequently focused on lower-chromium (1Cr, 2Cr, 3Cr, and 5Cr steels) in the liquid phase of SC CO_2. A chromium content of approximately 3 wt% is sufficient to effectively inhibit localized corrosion under these conditions.[22] The addition of Cr content causes the corrosion product film to change from a crystalline to an amorphous structure.[23] The amorphous $Cr(OH)_3$ corrosion product layer can pre-passivate the steel, thereby inhibiting corrosion.[24] Based on traditional low-Cr steel, Al further enhances its corrosion resistance by microalloying. In our previous work, we demonstrated that Fe–Cr–Al steel exhibits excellent corrosion resistance in SC-CO_2, particularly 3Cr2Al and 5Cr2Al,[25,26] which form a mixed corrosion product film of $Cr(OH)_3$ and $Al(OH)_3$. We have also studied the corrosion behavior of 3Cr2Al steel in SC CO_2 environment with 300 ppm SO_2. Even though the formation of a sulfur film has inhibited the corrosion, the corrosion rate is still not up to the ideal value.[27] Therefore, to fill the gap in these, corrosion behavior of 5Cr2Al steel will be further studied with 100 ppm/300 ppm SO_2 impurity. This will also further verify whether 5Cr2Al steel is suitable as a candidate material for CCS injection tubes.

In this paper, the liquid phase corrosion behavior and corrosion mechanism of X65 and 5Cr2Al steel containing 100 ppm and 300 ppm of SO_2 are compared. The interfacial corrosion behavior of X65 and 5Cr2Al was studied by *in situ* electrochemical methods, and their anodic and cathodic corrosion mechanisms were analyzed. The surface morphology of the corrosion products was thoroughly characterized by scanning electron microscopy (SEM), energy dispersive spectroscopy (EDS), X-ray diffraction (XRD), and X-ray photoelectron spectroscopy (XPS). The local corrosion rate of X65 and 5Cr2Al steel in supercritical CO_2 gas phase and water-rich phase was analyzed by laser scanning confocal microscopy (LSCM).

2. Experimental methods

2.1 Materials and solution

X65 steel blocks (80 mm long × 30 mm wide × 5 mm thick) were machined from commercial pipes. The novel Al-containing low-Cr steel was prepared based on conventional carbon steel by introducing 5 wt% Cr and 2 wt% Al, which was studied in our previous work.[25] Their chemical compositions are detailed in Table 2. The X65 and 5Cr2Al materials were machined into two-dimensional samples with the dimensions

Table 2 Chemical composition of X65 and 5Cr2Al steel (wt%)

Materials	C	Si	Mn	Cr	Mo	Al	S	Fe
X65	0.04	0.20	1.5	≤0.5	≤0.5	—	≤0.003	Bal.
5Cr2Al	0.05	0.20	0.55	5.00	0.15	2.00	≤0.003	Bal.

Table 1 Summary of literature on corrosion rates in supercritical CO_2 environments for various materials

Material	Temperature (K)	Pressure (MPa)	Time (h)	H_2O (ppmv)	Impurities	Corrosion rate (mm per year)	Ref.
X65	323.15	8	24	Sat.	—	10.8	Choi *et al.*[3]
			24	Sat.	0.33 MPa O_2	10.9	
			24	Liq.	—	19.2	
			24	Liq.	0.33 MPa O_2	19.3	
			120	Liq.	—	10.6	
			120	Liq.	0.33 MPa O_2	14.1	
13Cr	323.15	8	24	Sat.	—	∼0.01	
			24	Sat.	0.33 MPa O_2	∼0.01	
K03014	298.15	8	48	Sat.	200 ppm H_2S	0.07	Choi *et al.*[28]
	353.15	12	48	Sat.	200 ppm H_2S	0.41	
1Cr	298.15	8	48	Sat.	200 ppm H_2S	0.13	
	353.15	12	48	Sat.	200 ppm H_2S	0.44	
3Cr	298.15	8	48	Sat.	200 ppm H_2S	0.14	
	353.15	12	48	Sat.	200 ppm H_2S	0.55	
P110	353.15	9.5	168	Liq.	—	6.12	Zhang *et al.*[29]
N80	333.15	8	96	Liq.	—	12	Zhang *et al.*[30]
1Cr	333.15	10	192	Liq.	—	1.5	Hua *et al.*[31]
3Cr	333.15	10	192	Liq.	—	1.8	
5Cr	333.15	10	192	Liq.	—	2.0	
38Mn6/C75	353.15	13.5	96	Liq.	—	11	Zhang *et al.*[32]
Super 13Cr SS	473	2.85	120	Liq.	—	1.1	Yue *et al.*[33]

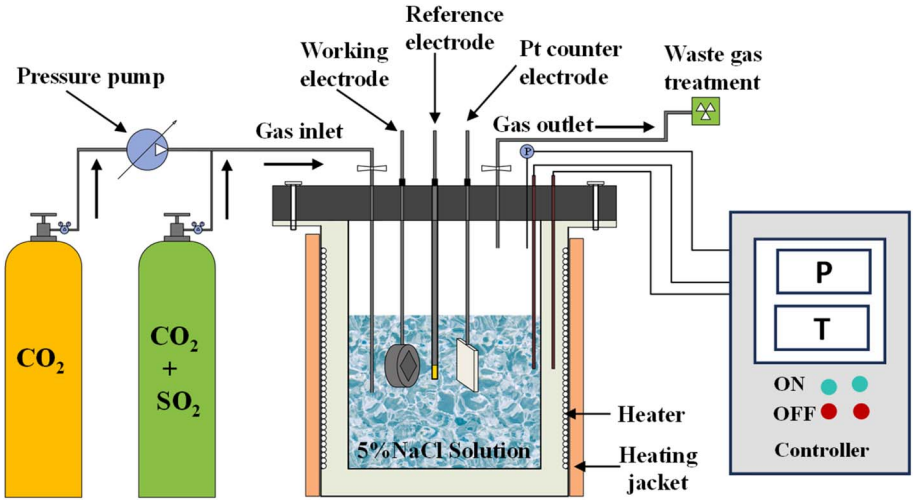

Fig. 1 Schematic diagram of the corrosion test device.

of 3 mm × 3 mm × 10 mm for surface and cross-sectional characterization and 3 mm × 10 mm × 20 mm for the weight loss measurements. Before the corrosion test, each sample was ground with silicon carbide paper of 400, 800, 1200, and 1500 grit, sequentially, then cleaned with deionized water and ethanol. After drying, the specimens were subsequently weighed using an electronic balance with a precision of 0.1 mg (M_{0i}) and measured with a Vernier caliper accurate to 0.01 mm. The test solution simulated a brine environment with a concentration of 5% NaCl. A 2 L NaCl solution was introduced into the autoclave.

2.2 Corrosion tests

The experiments were conducted in a 3 L high-temperature, high-pressure autoclave made of alloy 316L. Before the experiment, deoxygenate 2 L of 5% NaCl solution for 12 h by purging with 99.99% CO_2. Then the autoclave was sealed and degassed with CO_2 for 3 h. The temperature was increased to 80 °C. A mixture of CO_2 + 100/300 ppm SO_2 was charged (as shown in Fig. 1). Continue to pressurize with CO_2 to obtain a total pressure of 8 MPa. After exposure for 168 h, the samples were immediately rinsed with anhydrous ethanol and dried. Then the three parallel specimens were pickled according to the ASTM G1-03 standard. The pickling solution was prepared by dissolving 3.5 g of hexamethylene tetramine in 500 mL of hydrochloric acid, followed by dilution to a final volume of 1000 mL with deionized water. Then, the samples were cleaned for 10 minutes at 20–25 °C. Finally, these samples were rinsed, dried, and weighed again to obtain the final weight (M_{1i}). The corrosion rate was calculated according to:

$$V_{cr} = \frac{87\,600(M_{0i} - M_{1i})}{t\rho S} \quad (1)$$

where V_{cr} is the general corrosion rate in mm a^{-1}; M_{0i} and M_{1i} are the original and final weights of the specimen in g; t is the immersion time in hours; ρ is the steel density in g cm^{-3}; and S is the exposed surface area in cm^2.

2.3 Microstructure characterization and mechanical performance tests

Laser scanning confocal microscopy (LSCM) was employed to analyze the two-dimensional morphology and local corrosion conditions after pickling. The surface and cross-sectional morphologies of the corrosion products were characterized by scanning electron microscopy (SEM, ZEISS MERLIN COMPACT). The atomic composition and distribution were examined by energy dispersive X-ray spectroscopy (EDS). The acceleration voltage is 15 kV and the working distance is 10–15 mm in SEM and EDS. The atomic composition and atomic valence states of the corrosion products were analyzed respectively using X-ray diffraction (XRD, SMARTLAB) and X-ray photoelectron spectroscopy (XPS, ThermoFisher ESCALABXi+).

2.4 *In situ* electrochemical measurement

Electrochemical measurements were carried out using a Gamry Reference 600+ electrochemical workstation. A three-electrode electrochemical system was used with X65 and 5Cr2Al steel with an exposed area of 1 cm^2 as the working electrode (WE), platinum as the counter electrode (CE), and a high-temperature and high-pressure Ag/AgCl electrode as the reference electrode (RE). The schematic diagram of the autoclave and the position of WE, CE and RE were shown in Fig. 1. A digital pressure gauge was used to monitor autoclave pressure; a heat controller was applied to monitor and regulate the heating of the autoclave; and a saturated NaOH solution was used as a waste gas treatment device (shown in controller of Fig. 1). The Open circuit potential (OCP) was initially recorded for 1 h to ensure a stable OCP value (a fluctuation less than 5 mV for 2 minutes is considered stability). The polarization resistance (R_p) is obtained through the self-test method, that is, the slope in the linear polarization region is directly equal to the R_p. Electrochemical impedance spectroscopy (EIS) was measured at the OCP with 10 mV AC signals in the range of 0.01–100 000 Hz. The LPR experiments were performed at a scanning rate of

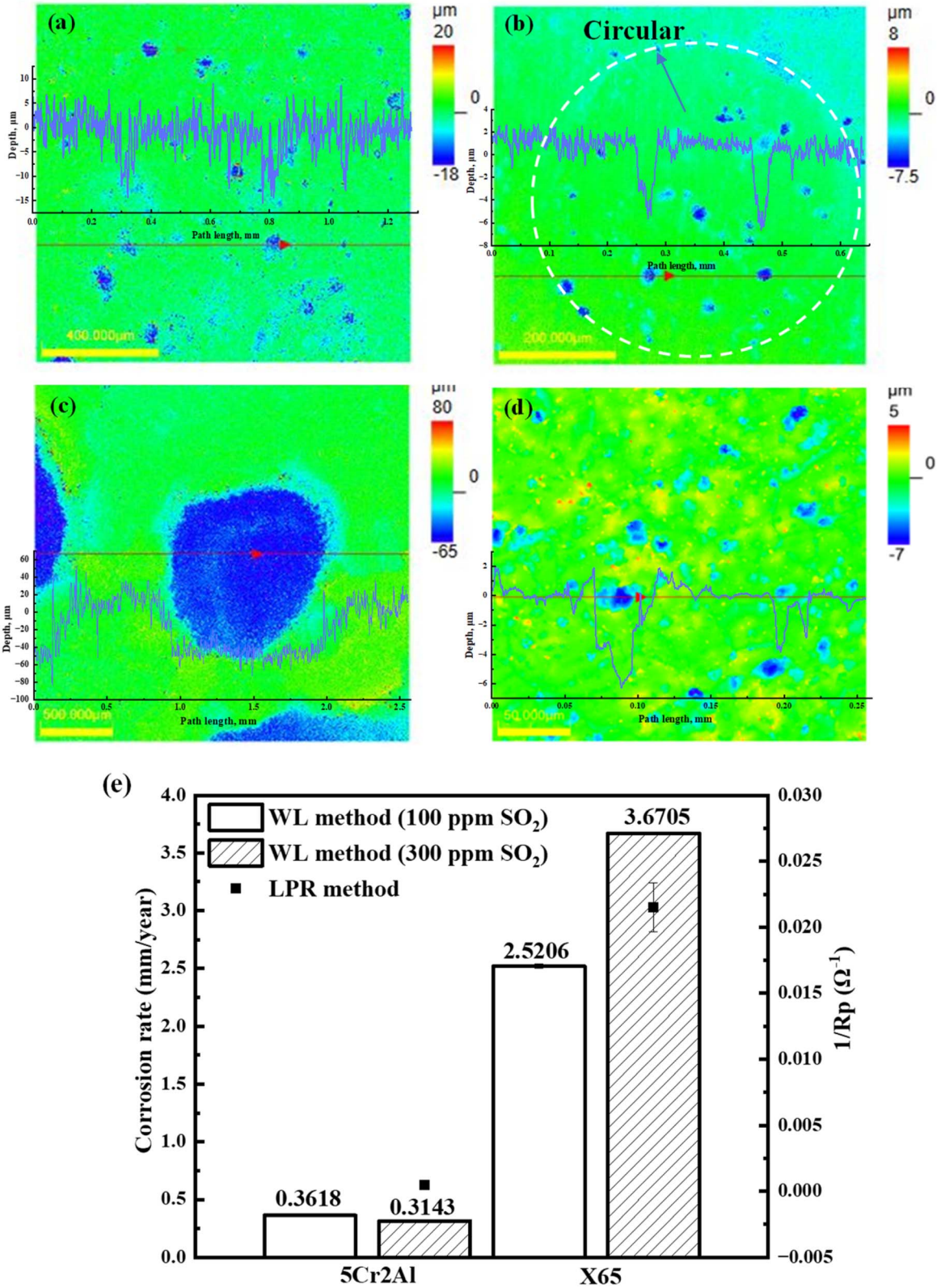

Fig. 2 2D characteristics of X65 and 5Cr2Al steel after acid pickling: (a) X65 steel, 100 ppm SO_2; (b) 5Cr2Al steel, 100 ppm SO_2; (c) X65 steel, 300 ppm SO_2; (d) 5Cr2Al steel, 300 ppm SO_2; (e) overall corrosion rates (note: WL: weight loss; LPR: line polarization resistance).

0.125 mV s^{-1} in the range of ±10 mV. The polarization curve test ranged from −300 mV to +400 mV *vs.* OCP at a scan rate of 0.1667 mV s^{-1}. The corrosion rate was obtained with eqn (2):

$$CR = \frac{i_{corr}(\mu A\ cm^{-2})EW(g)}{F \times \rho(g\ cm^{-3}) \times A(cm^3)} \quad (2)$$

where i_{corr} is the corrosion current density in "μA cm^{-2}"; E is the number of electrons lost; W is the molar mass in g; F is the Faraday constant; A is the exposed area of the test sample in cm^3; and ρ is the sample density in g cm^{-3}.

3. Results and discussion

3.1 Corrosion rate and macroscopic film characteristics

Fig. 2(a)–(d) shows the two-dimensional morphology of the X65 and 5Cr2Al steels observed after the removal of the corrosion products. Pitting corrosion of X65 and 5Cr2Al with 100 ppm SO_2 was 0.6257 and 0.2607 mm per year, respectively. In addition, 5Cr2Al presented a morphology similar to the corrosion circular pits in Fig. 3(b_1), with the pitting corrosion inside and at the edge of the circular pits being more severe than the external corrosion product coverage area. No pitting corrosion was observed on the X65 with 300 ppm SO_2 after pickling, but rather step-like corrosion pits. This does not mean that the X65 did not undergo pitting corrosion; it is just that the initially formed pitting corrosion expanded with the progress of corrosion and turned into larger local corrosion. This phenomenon can be explained in combination with the subsequent electrochemical test results. The average pitting corrosion rate of 5Cr2Al with 300 ppm SO_2 is 0.3426 mm per year. The pitting factor is defined as the ratio of the pitting rate to the overall corrosion rate. It is widely used to evaluate the severity and potential threat of localized corrosion to the structural integrity and safety of pipelines and tubing systems. Generally, a pitting factor greater than 5 can be considered a threat to the integrity of steel.[20] The pitting factor of 5Cr2Al in two conditions are lower than 1. It hardly poses a threat to the integrity of steel. Besides, 5Cr2Al steel undergoes pitting corrosion at the initial stage of $Cr(OH)_3$ and $Al(OH)_3$ formation, then turns into general corrosion, and no pitting corrosion occurs in the later stage.

Fig. 2(e) presents the overall corrosion rates and polarization resistance ($1/R_P$) of the X65 and 5Cr2Al steels under aqueous phase with 100 ppm and 300 ppm SO_2. The corrosion rates of the two types of steel with 300 ppm SO_2, measured by the weight loss (WL) method and the line polarization resistance (LPR) method, are comparable. Clearly, the corrosion rate of X65 is 2.5206 mm per year with 100 ppm SO_2. Then it reaches 3.6705 mm per year with 300 ppm SO_2. They are more than ten times higher than those of 5Cr2Al. The addition of SO_2 only promotes corrosion of X65 steel. The corrosion rate of 5Cr2Al in two environments are very low. With 100 ppm SO_2, it is 0.3618 mm per year; interestingly, it decreases to 0.3143 mm per year containing 300 ppm SO_2. This might be attributed to the protective sulfur film formed by the synergistic reaction of Cr, Al and SO_2. The content of 300 ppm of SO_2 might be the threshold of this synergistic reaction. 5Cr2Al could reduce corrosion by nearly 91% compared to X65. Consequently, it poses minimal corrosion threat. The formation mechanism of corrosion products of 5Cr2Al with 300 ppm SO_2 will be further discussed through electrochemical studies in the following text.

3.2 Surface and cross-sectional morphologies

Fig. 3 shows microscopic morphologies and EDS spectra of corrosion film for X65 and 5Cr2Al steels in the aqueous phase with 100 ppm and 300 ppm SO_2. The corrosion products in Fig. 3(a_1) is blocky, mainly composed of Fe and O (points A). Fig. 3(b_1) shows the morphologies and energy spectra of the double-layer structure, which revealed that the inner layer components are elemental Cr, O, Fe and Al (point C). The outer layer contains mainly Fe and O (points B), and a lower amount of

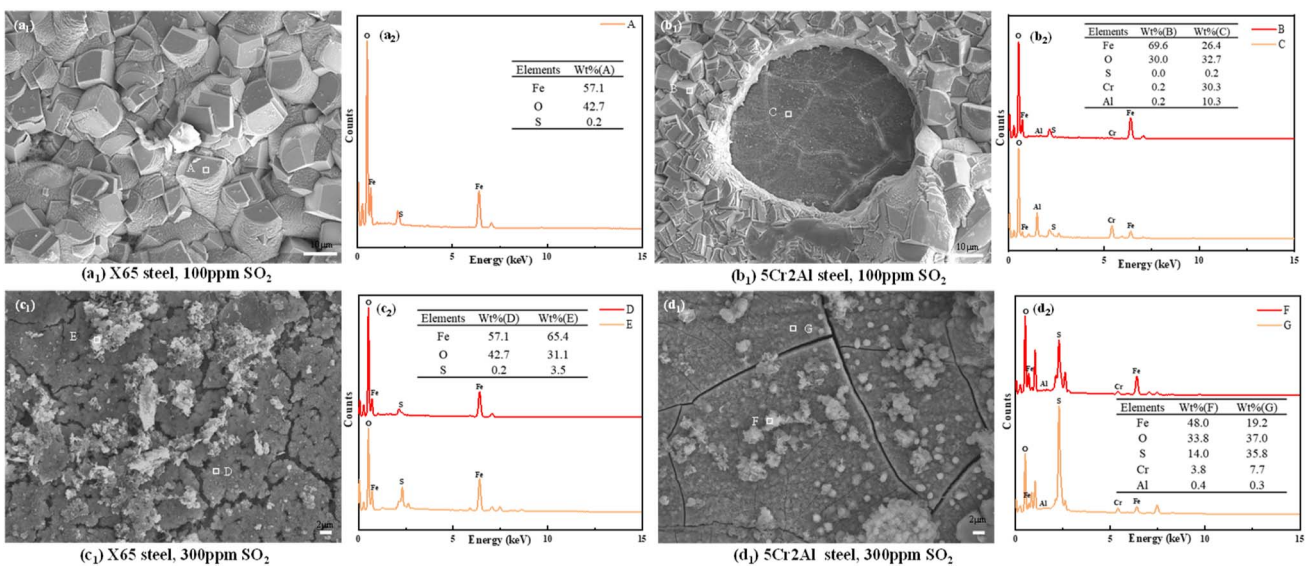

Fig. 3 SEM and EDS of X65 and 5Cr2Al steel exposed to aqueous phase at 8 MPa and 80 °C with different concentration of SO_2: (a_1)–(d_1) SEM images; (a_2)–(d_2) elemental composition of positions A–G.

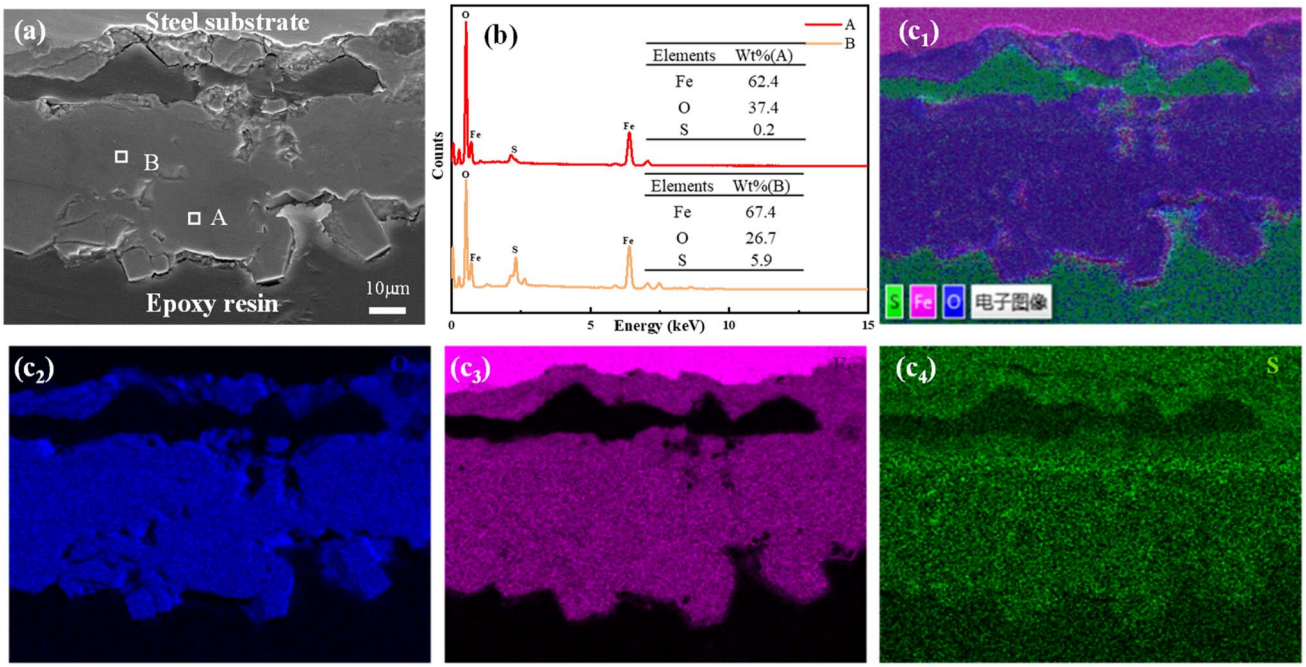

Fig. 4 Cross-sectional morphologies of X65 steel after exposure to aqueous phase with 300 ppm SO_2 at 8 MPa and 80 °C: (a) SEM images; (b) elemental composition of positions A and B; (c_1–c_4) elements surface scans.

sulfide was formed. As shown in Fig. 3(c_1), the whole surface was covered by loose products consisting of Fe and O (point D), which had cracks and cavities. It differs from the morphology in Fig. 3(a_1), with the corrosion product particles being finer. Obviously, Fig. 3(d_1) depicts a denser corrosion product than Fig. 3(c_1). The corrosion products were extremely fine and closely adhered to form an integral corrosion product film which was mainly composed of S and a small amount of Fe, O, Cr and Al (point G). This morphology also indicates superior corrosion resistance. There were a few free ions precipitated on the surface of the corrosion product film in the form of flocculent and spherical corrosion products. Furthermore, due to dehydration occurring during specimen extraction, fine micro-cracks were present on the surface of the corrosion product film.

Fig. 4 presents elemental map scanning for cross-sectional morphologies of X65 steel exposed to the aqueous phase with 300 ppm SO_2. The corrosion product layer with a thickness of about 86 μm exhibited the characteristic of irregular shape layer, containing Fe, O and S elements (Fig. 4). Epoxy entered the middle of the corrosion products through the cracks, as shown in the dark gray area in Fig. 4(a). According to the EDS point scan, there is only a small amount of S in the corrosion products, indicating that the main reaction occurred between Fe, CO_2 and water during immersion. However, the irregular morphology of the cross-sectional corrosion products suggests that SO_2 contributed to the local corrosion of the steel. Based on XRD and XPS, the main corrosion products of X65 steel in this environment are mainly $FeCO_3$, with a small amount of $FeSO_3$ and FeS.

Fig. 5 shows SEM images and EDS scans for cross-sectional morphologies of 5Cr2Al steel in the aqueous phase with 300 ppm SO_2. Compared with Fig. 4, the corrosion of 5C2Al steel in the CO_2–SO_2 system was much less. The corrosion product film consisted of a dense dark gray inner layer and a smooth light gray outer layer, with a thickness of about 9 μm (Fig. 5(a)). The thickness of the double-film layers is much smaller than that of X65. According to EDS line scan and surface scan, the inner dark grey layer is mainly composed of Cr, Al, and O, with a film thickness of approximately 3 μm; the outer light grey layer is mainly composed of S, with a film thickness of approximately 6 μm. Such a double-layer film structure effectively hinders the further development of the corrosion reaction. According to the EDS point scan (point B), the content of S is 67.1 wt%, and that of Fe is 12.8 wt%. The atomic ratio of S: Fe is approximately 9.5. It is much higher than that of FeS. This indicates that the outer sulfur film is composed of a large amount of elemental sulfur. The presence of SO_2 induced a change in the film structure, forming a dense, integral, and uniform protective sulfur film of a certain thickness on the surface of the original $Cr(OH)_3$ and $Al(OH)_3$ layers, which inhibited the further progression of corrosion. Obviously, X65 cannot form such an integral and dense S layer.

3.3 XRD analysis

Further analysis in combination with Fig. 6, Strong $FeCO_3$ peaks were detected in the X65 in two conditions, which should coincide with the element concentrations analyzed in the EDS point scan (Fig. 3). $FeCO_3$ was the main corrosion product in the aqueous phase.[34] Besides the diffraction peaks of $FeCO_3$, a small amount of sulfides was also detected in the X65. Notably, for 5Cr2Al, an increase in SO_2 content makes the corrosion products more complex. Compared to 100 ppm SO_2, in addition to the diffraction peaks assigned to the Fe–Cr base, $FeCO_3$, and sulfides, there is also elemental sulfur present. The result is consistent with the EDS result in Fig. 5. XRD can only be applied to the detection of

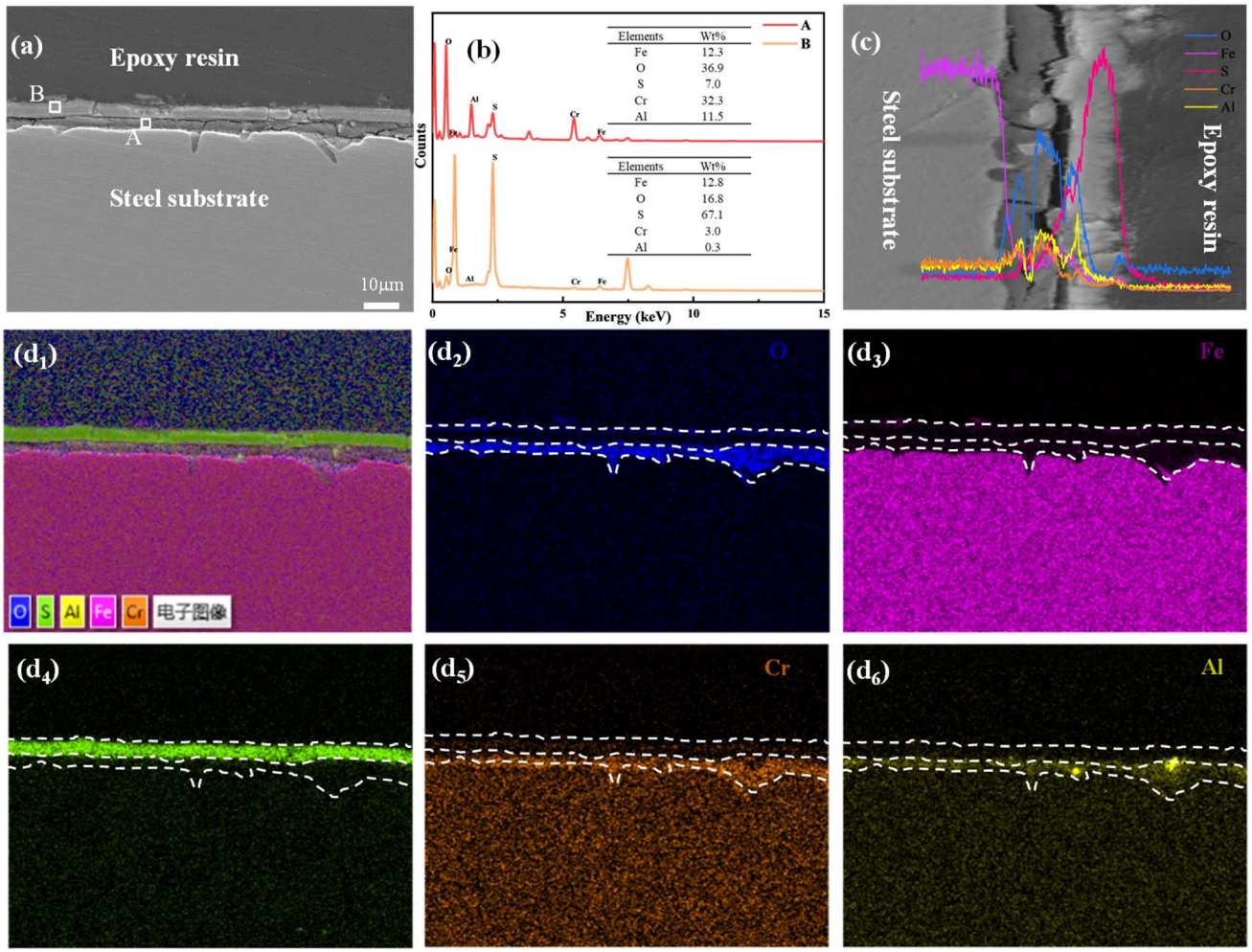

Fig. 5 Cross-sectional morphologies of 5Cr2Al steel exposed to aqueous phase with 300 ppm SO_2 at 8 MPa and 80 °C: (a) SEM images; (b) elemental composition of positions A and B; (c) elements line scan; (d_1–d_6) elements surface scans.

crystalline substances. XPS can detect both crystalline and amorphous corrosion products. We used XPS to conduct further analysis on the corrosion products of these two types of samples.

3.4 XPS analysis

Fig. 7 show a high-resolution XPS spectrum of the corrosion scale of X65 and 5Cr2Al with 300 ppm SO_2. To ensure that all

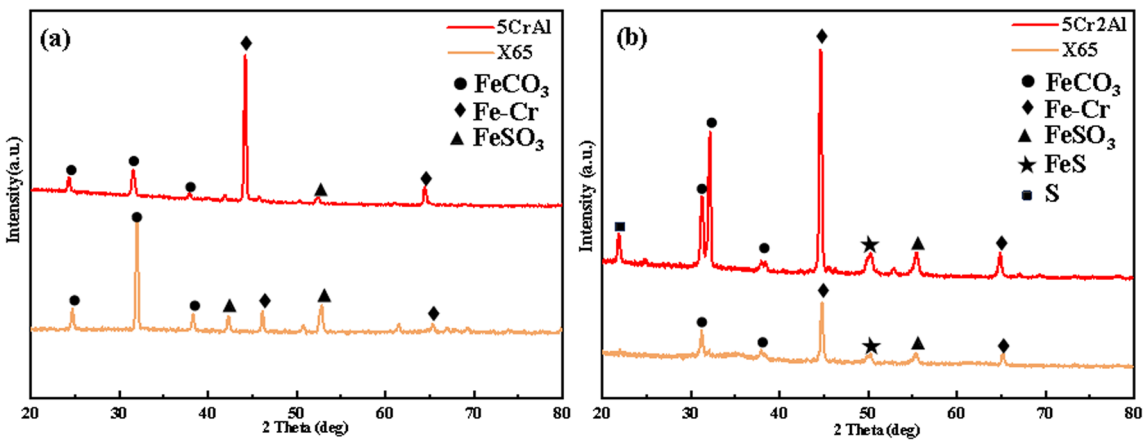

Fig. 6 XRD spectra of the corrosion products formed on X65 and 5Cr2Al steel after exposure to aqueous phase for 168 h at 8 MPa and 80 °C: (a) with 100 ppm SO_2; (b) with 300 ppm SO_2.

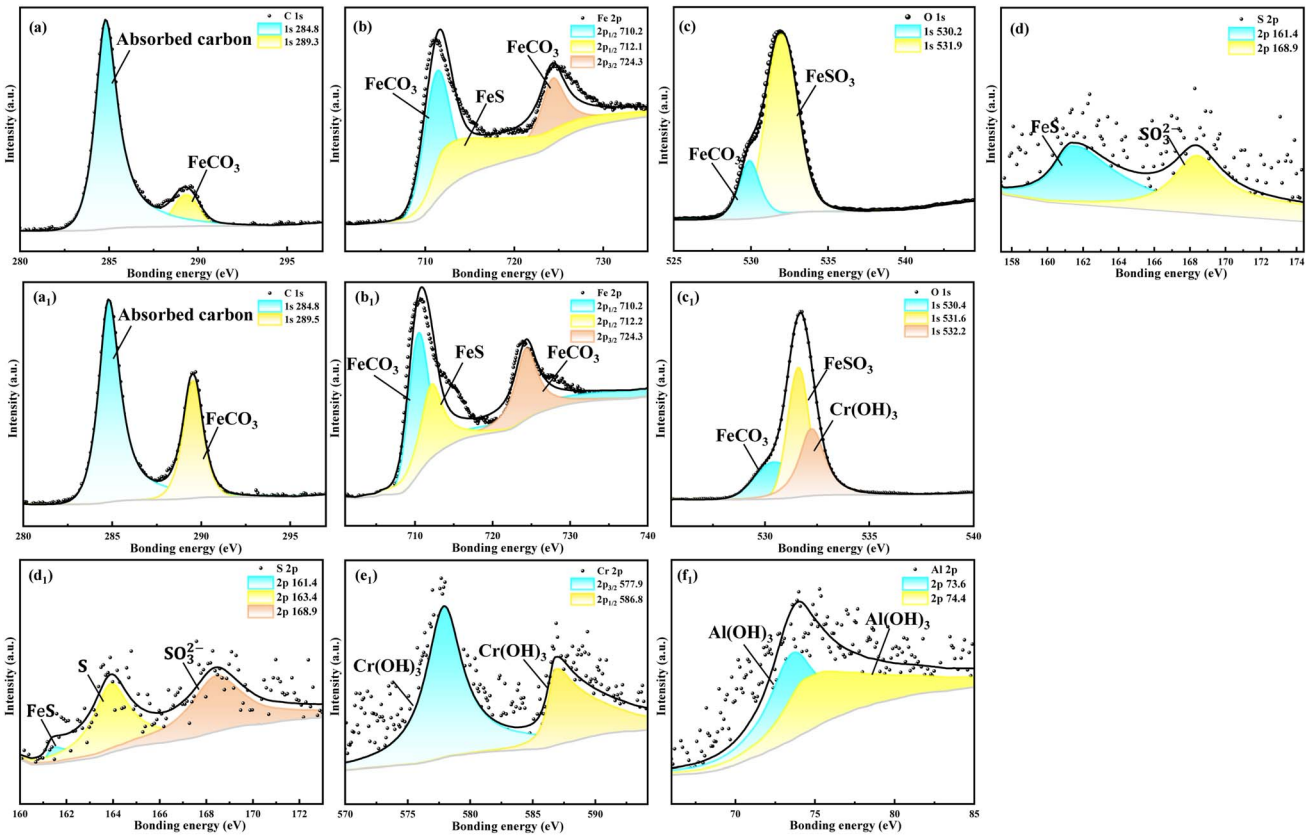

Fig. 7 XPS spectra and peaks deconvolution for various elements of the corrosion product formed on X65 ((a)–(d)) and 5Cr2Al ((a$_1$)–(f$_1$)) steel.

types of corrosion products could be detected, the corrosion products were ground into a fine powder and subsequently analyzed by XPS. As shown in Fig. 7((a)–(d)), the C 1s peaks with the binding energy of 284.8 eV correspond to adsorbed carbon. The C 1s peak at 289.3 eV, the O 1s peak at 530.2 eV, the Fe 2p$_{1/2}$ peak at 710.2 eV, and the Fe 2p$_{3/2}$ peak at 724.3 eV were related to $FeCO_3$.[35] The O 1s peak at 531.9 eV and the S 2p peak at 168.9 eV could be assigned to $FeSO_3$.[36,37] Meanwhile, the S 2p peak at 161.4 eV and Fe 2p$_{1/2}$ peak at 712.1 eV were correlated to the existence of FeS.[36,37] Therefore, combining the XRD analysis, the atom ratio of EDS, and XPS results, the main components of X65 steel corrosion products were $FeCO_3$, $FeSO_3$, and FeS.

As shown in Fig. 7((a$_1$)–(f$_1$)), the C 1s peaks at binding energies of 284.8 eV and 288.4 eV corresponded to adsorbed carbon and $FeCO_3$, respectively.[38,39] The O 1s spectrum at the binding energies of 530.4 eV, 531.6 eV and 531.9 eV corresponded to $FeCO_3$, $FeSO_3$ and $Cr(OH)_3$,[38] respectively. The Fe 2p spectrum was fitted with three peaks: two components assigned to Fe 2p$_{1/2}$ (724.3 eV) and Fe 2p$_{3/2}$ (710.2 eV) that were both typical of $FeCO_3$,[38] and an additional Fe 2p$_{1/2}$ peak (712.2 eV) associated with FeS.[36,37] For S 2s, besides the peaks assigned to $FeSO_3$ (168.9 eV)[40] and FeS (161.4 eV), a peak appeared at 163.4 eV, which was related to S.[36,37] Additionally, for 5Cr2Al, the Al 2p$_{3/2}$ peak at 73.9 eV and Al 2p$_{1/2}$ peak at 74.7 eV indicated the presence of $Al(OH)_3$.[41] The Cr 2p$_{3/2}$ peak at 577.9 eV, the Cr 2p$_{1/2}$ peak at 586.8 eV, and the O 1s peak at 532.2 eV indicated the formation of $Cr(OH)_3$.[42,43] Based on the XRD analysis, the atom ratio of EDS, and XPS results, it was concluded that the corrosion products consisted of $Cr(OH)_3$, $Al(OH)_3$, $FeCO_3$, $FeSO_3$, FeS, and S for 5Cr2Al.

3.5 Potentiodynamic polarization measurements

From the previous manifestations, due to the low content of 100 ppm SO_2, only a small amount of sulfides was formed. 300 ppm SO_2 formed a sulfur elemental layer in 5Cr2Al steel. To further explore the underlying mechanisms of the formation of

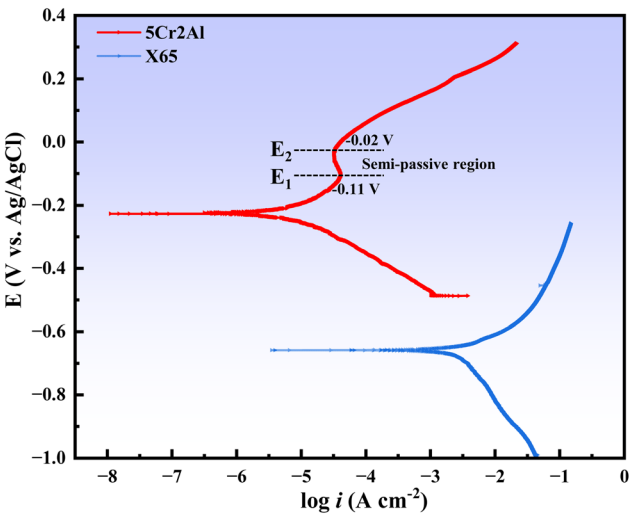

Fig. 8 Polarization curve of 5Cr2Al and X65 steel exposed in water-rich phases with 300 ppm SO_2 at 8 MPa CO_2 and 80 °C for 168 h.

Table 3 Electrochemical parameters of polarization curves of 5Cr2Al and X65 steel exposed in water-rich phases with 300 ppm SO_2 at 8 MPa CO_2 and 80 °C for 168 h

Conditions	E_{corr} (mV *vs.*)	R_P (Ω cm^{-2})	i_{corr} (A cm^{-2})	CR (mm per year)
X65	−0.64969	46.5	0.002849	3.3172
5Cr2Al	−0.0444	2287.1	0.0000317	0.369

sulfur, polarization curves were measured with X65 and 5Cr2Al when containing 300 ppm SO_2 (Fig. 8). Compared with X65, the OCP of 5Cr2Al moves in a positive direction, shifting from −0.66 V to −0.22 V, and the overall polarization curve shifts to the left. Both the cathodic and anodic processes occurring near the corrosion potential are simultaneously inhibited, leading to a reduced corrosion current. 5Cr2Al exhibits an obvious semi-passivation phenomenon, which is characterized by a decrease in current between E_1 (−0.11 V *vs.* Ag/AgCl) and E_2 (−0.02 V *vs.* Ag/AgCl). It is not present in the X65 steel without Cr and Al. The semi-passivation phenomenon of 5Cr2Al is related to the formation of $Cr(OH)_3$, $Al(OH)_3$ and a dense sulfur layer. Table 3 shows that the corrosion current density of 5Cr2Al is two orders of magnitude smaller than that of X65. The R_p of 5Cr2Al is 50 times that of X65 (the value of R_p is self-measured), indicating that the corrosion product film formed on 5Cr2Al has better protective properties. The corrosion rate can be calculated from the corrosion current density, which is consistent with the conclusion obtained by the weight loss method. The corrosion rate of X65 is about 10 times that of 5Cr2Al.

3.6 EIS measurements

To reveal the differences in corrosion mechanism and micromorphologies between X65 and 5Cr2Al with 300 ppm SO_2, impedance spectroscopy was employed to analyze the formation process of corrosion product films on the two materials. Fig. 9(a_1)–(f_1) presents the EIS results obtained for X65 steel after different immersion times (1–168 h) under conditions of 8 MPa and 80 °C. In the initial stage of corrosion (1–3 h), X65 steel is characterized by a capacitive loop at a high frequency, an inductive loop at an intermediate frequency, and a capacitive loop at a low frequency, which represent three time constants.

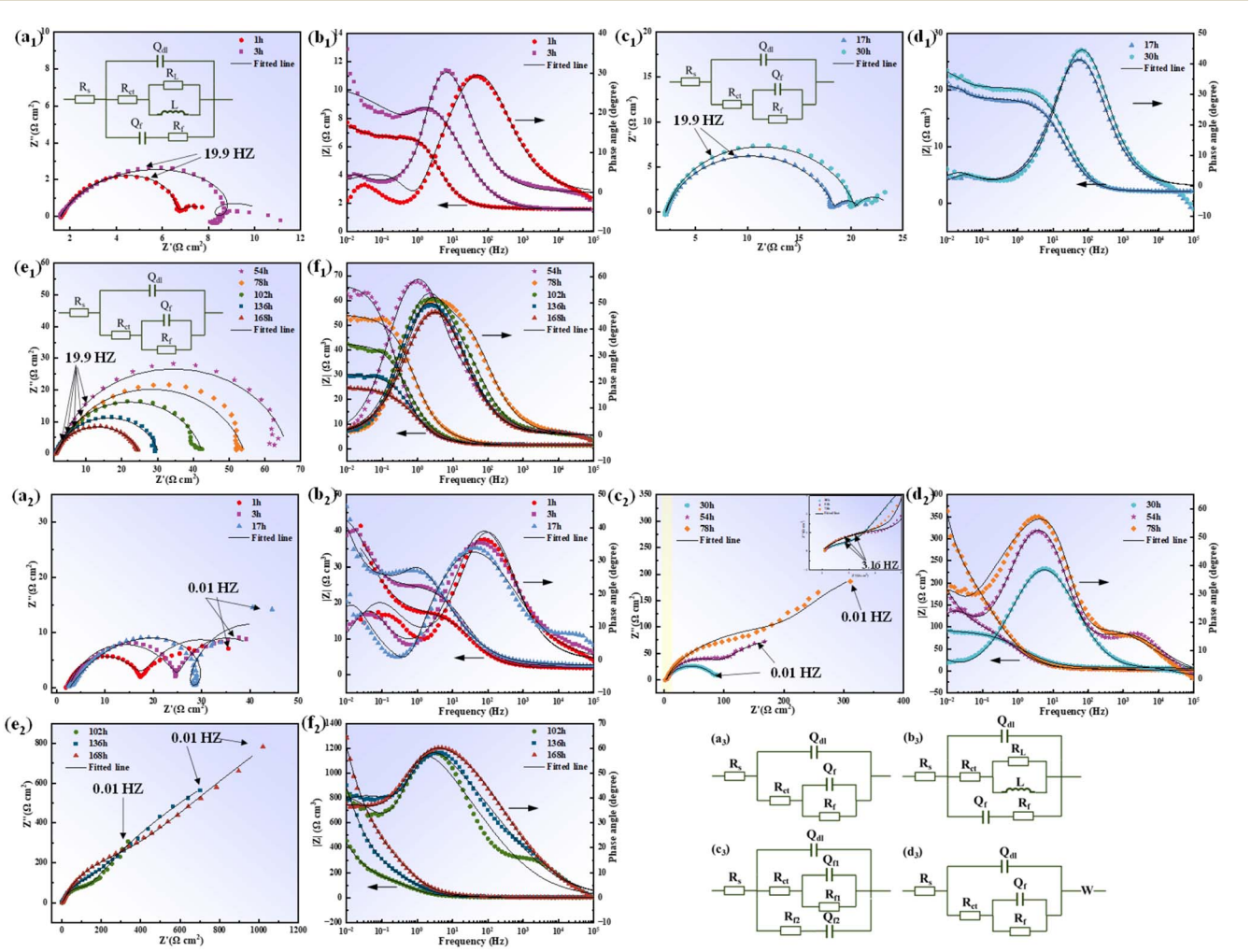

Fig. 9 EIS of steel immersed in aqueous phases at different corrosion periods at 8 MPa and 80 °C with 300 ppm SO_2: (a_1)–(f_1) Nyquist and Bode plot for 1–168 h of X65; (a_2)–(f_2) Nyquist and Bode plot for 1–168 h of 5Cr2Al; (a_3)–(d_3) equivalent circuits for EIS fitting of 5Cr2Al steel ((a_3) 1–3 h; (b_3) 17 h; (c_3) 30–78 h; (d_3) 78–168 h).

The capacitive loop observed at high frequencies can be attributed to the double-layer capacitance and the charge transfer resistance.[44] The appearance of the medium-frequency inductive loop is due to the local adsorption of OH^- on the steel surface to form the intermediate product $FeOH_{ads}$ and the occurrence of pitting corrosion.[45,46] The capacitive loop observed at low frequencies may be associated with the formation of a corrosion product film.[44] As the exposure time increases, the diameters of the high-frequency capacitive loop and the low-frequency capacitive loop increase. Then the inductive loop is observed to disappear, with only the high-frequency and low-frequency capacitive loops remaining (17–30 h). The middle and late stages of corrosion (54–168 h) are characterized by two time constants, *i.e.*, a high-frequency capacitive loop and a low-frequency capacitive loop. Interestingly, the diameter of the capacitive loop reaches its maximum at 54 h, and gradually decreases as the corrosion progresses. This indicates that the corrosion products formed on X65 steel, mainly ferrous carbonate, provide very poor protection.

Table S1 lists the fitted parameters obtained from the EIS data with equivalent circuits. The equivalent circuit diagram of the corresponding impedance spectrum is placed in Nyquist. The model elements are defined as follows: R_s is the solution resistance; R_{ct} is the charge-transfer resistance; R_f is the corrosion-product film resistance; Q_{dl} and Q_f are constant-phase elements corresponding to the double-layer capacitance and the film capacitance, respectively; L is the inductance; and R_L is the inductance resistance. It can be seen from Table S1 that the polarization resistance ($R_{ct} + R_f$) increased from 6.26 Ω cm^2 at 1 h to 67.05 Ω cm^2 at 54 h. The charge transfer was slow and the corrosion process was inhibited. Then the polarization resistance gradually decreased with prolongation of exposure time, dropping to a value of 23.08 Ω cm^2 at 168 h. The diameter of the capacitive loop first increased and then decreased with time, indicating that the corrosion process was controlled by charge transfer. In the initial stage of corrosion, the steel dissolved. The formed corrosion products were relatively loose (Fig. 3(c_1) and 4), providing poor protection, and thus the impedance value was small. During the middle stage, the thickness of the corrosion product film gradually increases, thereby enhancing its protective effect and increasing the impedance value. However, the impedance value gradually decreases in the later stage due to the continuous growth of the corrosion product film to a critical thickness, after which the film breaks. This indicates that the $FeCO_3$ film has almost a non-protective nature in the later stage of corrosion, and the corrosion rate increases rapidly.

EIS measurements of 5Cr2Al, in the Nyquist and Bode format, are shown in Fig. 9(a_2)–(f_2). At the initial stage, it is characterized by two time constants, one capacitive loop at high frequency, and one capacitive loop at low frequency. With the prolongation of exposure time, the diameter of the impedance loop increases. Subsequently, the inductive loop appears (17 h). Pitting occurs in the initial stage, and no pitting occurs in the later stage. As the corrosion progresses, during the mid-stage of corrosion (30–78 h), the inductive loop disappears and is characterized by three time constants: one capacitive loop at high frequency, one capacitive loop at intermediate frequency, and one capacitive loop at low frequency. Due to the accumulation of a certain thickness of $Cr(OH)_3$ and $Al(OH)_3$ layers, the diameter of the impedance loop increases by an order of magnitude, and the low-frequency impedance loop gradually approaches the Warburg impedance. In the final stage (102–168 h), the Warburg impedance response becomes clearly distinguishable. This stage is characterized by two time constants. In the previous stage, the first and second capacitive loops merged into one due to their similar time constants, and a Warburg impedance (45° straight line) emerged. Warburg impedance is a diffusion-controlled process that corresponds to pure diffusion with an infinite diffusion layer. The emergence of the Warburg impedance indicates that the system begins to be dominated by diffusion, showing a typical linear diffusion tail in the low-frequency region, and the overall corrosion rate is very slow. According to the previous EDS morphology analysis, it is known that in an environment containing SO_2, 5Cr2Al forms a dense sulfur film. Surprisingly, it acts as a diffusion barrier, with a very small W and an impedance loop diameter reaching four orders of magnitude. Therefore, the increase in impedance is due to the growth of the sulfur film. The high-frequency capacitive loop is associated with the cathodic and anodic reactions occurring on the surface of the solution and corrosion products. The medium-frequency capacitive loop may be associated with the occurrence of pitting corrosion and the adsorption of intermediate products. The low-frequency capacitive loop is related to the corrosion product film. The Warburg impedance corresponds to the diffusion-limited process.

Table S2 lists fitted parameters obtained from the EIS data with the corresponding equivalent circuit. The equivalent circuits for 1–3 h, 17 h, 30–78 h and 102–168 h are fitted by Fig. 9(a_3)–(f_3), respectively. Additionally, W represents the Warburg impedance, which is caused by diffusion of the transferred substance and becomes very obvious after the formation of the sulfur film. Table S2 shows that in the initial corrosion stage (1–17 h), the corrosion reaction occurs rapidly with small R_{ct} and R_f values, but the overall polarization resistance value increases. In the middle stage (30–78 h), the polarization resistance value rapidly increases to 496.88 Ω cm^2. Combined with the EDS surface scan analysis, this is due to the rapid growth of the inner layer of $Cr(OH)_3$ and $Al(OH)_3$ corrosion products, resulting in an accumulation of thickness. In the later stage (102–168 h), the diffusion polarization impedance value reached 2937.47 Ω cm^2, and the Warburg impedance value was 0.0085. The large diffusion impedance indicates that the formation of the sulfur film in the later stage greatly inhibited the diffusion-dominated corrosion. The overall reaction rate was very slow, and only a very small amount of ions could pass through the sulfur film and the $Cr(OH)_3$ and $Al(OH)_3$ barriers to exchange substances with the steel substrate.

3.7 Discussion of the corrosion mechanism

For X65 steel, when SO_2 dissolves in water, it generates sulfurous acid and other substances, lowering the pH of the solution and encouraging anodic dissolution.

$$SO_2 + H_2O \rightarrow HSO_3^- + H^+ \quad (3)$$

$$HSO_3^- \rightarrow SO_3^{2-} + H^+ \quad (4)$$

In an anaerobic environment, besides the formation of SO_3^{2-}, the addition of SO_2 also led to the formation of FeS. The specific reactions for the formation of FeS are shown in the reaction eqn (5)–(11).[47–49] Research[50] indicated that FeS has certain electrical conductivity and a positive potential relative to the steel substrate. The potential difference between the two will promote corrosion. For X65 steel, the addition of SO_2 promotes corrosion.

$$SO_2 \rightarrow SO_3^- \rightarrow S_2O_4^- \rightarrow S_4O_6^- \rightarrow S_2O_3^- \rightarrow S \rightarrow S_5^- \rightarrow S_4^- S_3^- \rightarrow S_2^- \rightarrow S^- \quad (5)$$

$$2SO_3^{2-} + 2H_2O + 2e^- \rightarrow S_2O_4^{2-} + 4OH^+ \quad (6)$$

$$2S_2O_4^{2-} + 2H_2O + 2e^- \rightarrow S_4O_6^{2-} + 4OH^+ \quad (7)$$

$$HS_2O_4^- \rightarrow S + SO_4^{2-} + H^+ \quad (8)$$

$$S_4O_6^{2-} + 2e^- \rightarrow 2S_2O_3^{2-} \quad (9)$$

$$S_2O_3^{2-} + H^+ \rightarrow S + SO_2 + H_2O \quad (10)$$

$$Fe + S \rightarrow FeS \quad (11)$$

Besides, in SC CO_2 environment, the cathodic process may include the reduction of H^+, H_2CO_3, HCO_3^-.[51]

$$2H^+ + 2e^- \rightarrow H_2 \quad (12)$$

$$2H_2CO_3 + 2e^- \rightarrow 2HCO_3^- + H_2 \quad (13)$$

$$2HCO_3^- + 2e^- \rightarrow 2CO_3^{2-} + H_2 \quad (14)$$

The anodic reaction is the oxidation of Fe:

$$Fe \rightarrow Fe^{2+} + 2e^- \quad (15)$$

When the concentrations of Fe^{2+} and CO_3^{2-} exceed the solubility product of $FeCO_3$ ($K_{sp} = 3.13 \times 10^{-11}$), $FeCO_3$ precipitation occurs. Although SO_2 lowers the pH and to some extent inhibits the hydrolysis of H_2CO_3, the corrosion process is mainly controlled by CO_2 in a CO_2 atmosphere. With the increase in impurity SO_2 content, the nucleation sites of $FeCO_3$ increase, resulting in finer grains. Thus, the corrosion product layer consists mainly of $FeCO_3$ for X65 steel. Additionally, sulfides promote the anodic dissolution of the steel, resulting in the formation of more Fe^{2+}, which makes it easier to occur the reaction of eqn (16).[52] Furthermore, when the SO_2 concentration increases from 100 ppm to 300 ppm, the formed $FeCO_3$ corrosion product becomes finer and the corrosion rate increases. In CO_2-300 ppm SO_2 system, we have learned through electrochemical research that the formation of $FeCO_3$ plays a protective role, which leads to an increase in the diameter of the impedance loop in the initial and middle stages. In the later stages, the formation of $FeCO_3$ mixed with sulfides, which is characterized by being loose and porous (Fig. 3c$_1$) and having a certain degree of conductivity, accelerates the corrosion. The amplitude of the impedance loop weakens, and the charge transfer process is considered to accelerate the cathodic process.[46,53] The decrease in R_f indicates that the weakened protective effect of the corrosion product film increases with immersion time. In addition, the anodic polarization curve is very smooth, indicating that no passive film is formed.

$$Fe^{2+} + CO_3^{2-} \rightarrow FeCO_3 \quad (16)$$

For 5Cr2Al steel in a CO_2-100 ppm SO_2 system, there is a higher reactivity of Cr and Al compared to Fe. Thus, Cr and Al dissolve preferentially (eqn (17) and (18)).[54] K_{sp} ($Al(OH)_3$) = 1.3×10^{-33}, K_{sp} ($Cr(OH)_3$) = 6.3×10^{-31}, K_{sp} ($FeCO_3$) = 3.13×10^{-11}. Due to the smaller K_{sp} of $Cr(OH)_3$ and $Al(OH)_3$, they precipitate preferentially, forming a thin layer of $Cr(OH)_3$ and $Al(OH)_3$ (eqn (19) and (20)). An outer layer of corrosion products is mainly composed of $FeCO_3$ (Fig. 3(b$_1$)). In a CO_2-300 ppm SO_2 system, an increase in SO_2 content with Cr and Al elements alters the type of corrosion products, which is not observed in X65 steel without Cr and Al. It also forms a layer of $Cr(OH)_3$ and $Al(OH)_3$ (Fig. 5). Based on the electrochemical data analysis, the impedance loop initially shows a double capacitive loop, indicating that the formed $Cr(OH)_3$ and $Al(OH)_3$ are protective. Cr and Al continuously precipitate with exposure time, forming a $Cr(OH)_3$ and $Al(OH)_3$ layer with a thickness of 3 μm. The pH value near the steel surface will decrease.[24] In an anaerobic environment, SO_2 will also cause the reactions of eqn (3) and (4). The pH will also decrease accordingly. In a lower pH environment, the ionization of H_2CO_3 is almost inhibited, so there is almost no formation of $FeCO_3$ (Fig. 5). When the pH reaches the conditions for sulfite ion to occur the reactions of eqn (5)–(10), a large amount of elemental sulfur is formed, and the sulfur film blocks the exchange of substances between the steel substrate and the solution. It effectively hinders the diffusion of Fe^{2+}, Cr^{2+}, and Al^{2+} from the oxide film/matrix interface to the oxide film/solution interface, and reduces the concentration of ions above the inner oxide film. Correspondingly, the impedance loop gradually shows the Warburg impedance. At this time, the R_f also reaches four orders of magnitude, which indicates an artefact of the slow migration of species to and from the sulfur film surface. The formation of this more protective film leads to a semi-passivation phenomenon in the corresponding polarization curve.

$$Cr \rightarrow Cr^{3+} + 3e^- \quad (17)$$

$$Al \rightarrow Al^{3+} + 3e^- \quad (18)$$

$$Cr^{3+} + 3H_2O \leftrightarrow Cr(OH)_3 + 3H^+ \quad (19)$$

$$Al^{3+} + 3H_2O \leftrightarrow Al(OH)_3 + 3H^+ \quad (20)$$

We used the OLI software to calculate the solubility of 300 ppm SO_2 at different temperatures and pressures (Fig. 10). In the aqueous phase, it can be observed that CO_2 dissolved in the solution increases with pressure and decreases with temperature. This indicates that the solubility of CO_2 in water increases as pressure increases, and it decreases as temperature

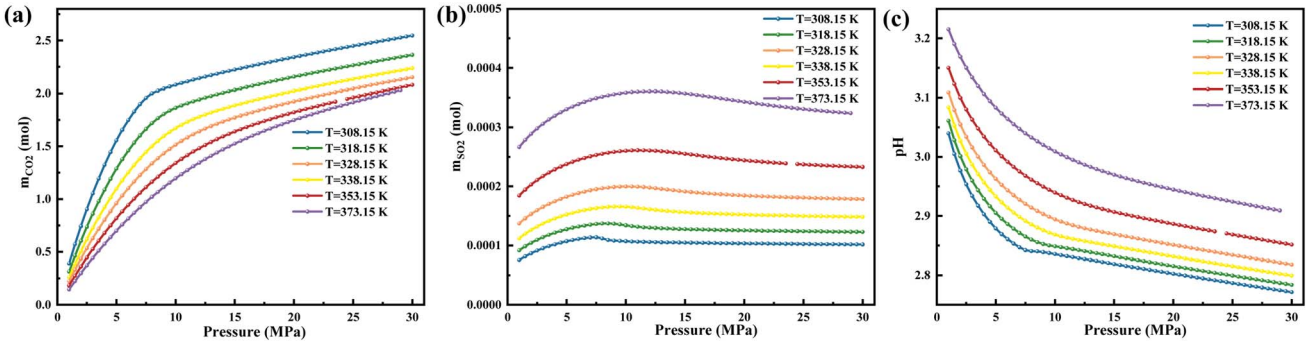

Fig. 10 The concentrations of CO_2 and SO_2 dissolved in water and the variation of pH with temperature and pressure: (a) CO_2; (b) SO_2; (c) pH.

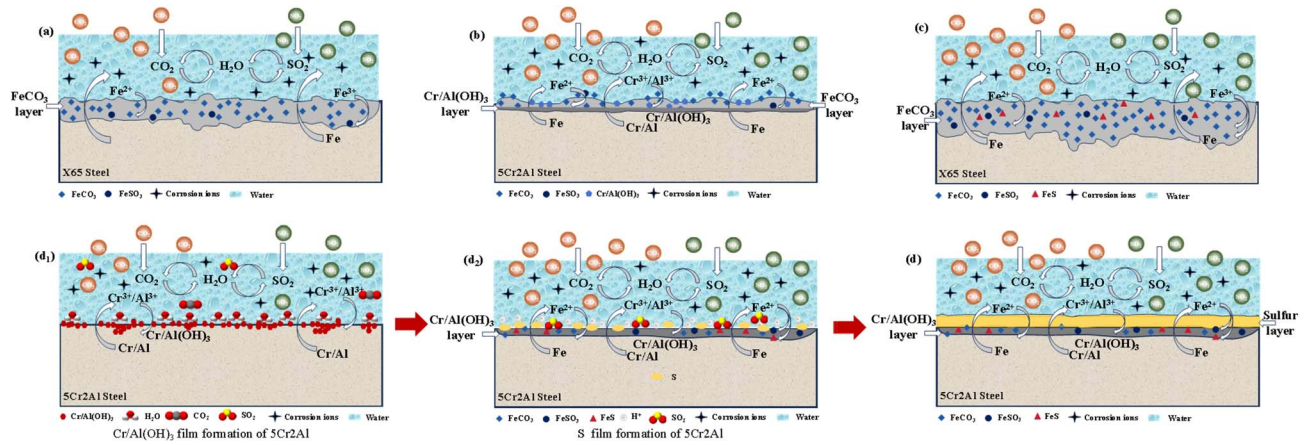

Fig. 11 Schematic diagram of corrosion film formation: (a) X65 with 100 ppm SO_2; (b) 5Cr2Al steels with 100 ppm SO_2; (c) X65 with 300 ppm SO_2; (d) 5Cr2Al with 300 ppm.

rises. The calculated trends are consistent with the findings of previous studies.[55] However, the solubility of SO_2 in water shows an opposite trend. It increases first and then decreases with the increase of pressure, and increases with the increase of temperature. The pH gradually decreases as pressure increases, which is related to the dissolution of more CO_2. When the pressure is lower than 8 MPa, the pH drops more rapidly, which is associated with the dissolution of more SO_2 at this time. The pH increases with the rise in temperature, which is related to the variation trend of CO_2 solubility with temperature. In this study, approximately 0.00026 mol of SO_2 was dissolved in water, almost reaching the dissolution peak, which made a great contribution to the reduction of pH. Additionally, due to the precipitation of Cr and Al in 5Cr2Al steel and their combination with water, the pH would be further reduced to a greater extent, which would be conducive to the formation of a sulfur film.

The corrosion mechanism model of X65 and 5Cr2Al steel in aqueous phases with 100 ppm and 300 ppm SO_2 at a total pressure of 8 MPa and 80 °C are shown in Fig. 11. The corrosion mechanism of the two types of steel with 100 ppm and 300 ppm SO_2 shows significant differences. In a CO_2-100 ppm SO_2 system, X65 undergoes a reaction dominated by the formation of $FeCO_3$. A small amount of sulfides is also produced (Fig. 11(a)). The inner layer of 5Cr2Al consists of a thin film of $Cr(OH)_3$ and $Al(OH)_3$ corrosion products (Fig. 11(b)). Given the minimal impact of 100 ppm SO_2 on pH, the precipitation of $FeCO_3$ is hardly inhibited, resulting in an outer layer predominantly composed of dense $FeCO_3$ with minor sulfide inclusions. In a CO_2-300 ppm SO_2 system, SO_2 merely accelerates the corrosion of X65 steel, and the type of corrosion products remains unchanged (Fig. 11(c)). However, for 5Cr2Al steel, the type of corrosion products changed, forming a double-layer structure with $Cr(OH)_3$ and $Al(OH)_3$ as the inner layer and elemental S as the outer layer, which inhibited the progress of corrosion (Fig. 11(d)–(d_2)). We found that only when Cr and Al are present and the SO_2 concentration reaches 300 ppm can a dense S elemental film be formed compared to 100 ppm SO_2.

4. Conclusions

(1) In the CO_2-100 ppm SO_2 system, X65 occur a reaction dominated by the formation of $FeCO_3$. SO_2 significantly accelerates both general and localized corrosion of X65 steel compared to 5Cr2Al steel. 5Cr2Al forms a double-layer structure with $Cr(OH)_3$ and $Al(OH)_3$ as the inner layer and $FeCO_3$ as the outer layer.

(2) In the CO_2-300 ppm SO_2 system, the corrosion rate of X65 is 1.5 times greater than that at 100 ppm. The corrosion

products formed on X65 steel have a certain protective effect in the initial and middle stages. However, in the later stage, the corrosion product layer loses its protective property due to its porous and loose structure as well as crack formation. SO_2 only accelerates corrosion in X65 without added Cr and Al.

(3) 300 ppm SO_2 is a concentration that will have a synergistic reaction with Cr and Al. It changes the corrosion mechanism and enhances the corrosion resistance of steel. This study found that only when Cr and Al are present and the SO_2 content reaches 300 ppm can a synergistic effect occur, which inhibits corrosion attack on the steel surface by forming a dense sulfur film on the outer surface of the thin $Cr(OH)_3$ and $Al(OH)_3$ layers.

(4) 5Cr2Al can reduce corrosion by nearly 91% when compared to X65. Therefore, 5Cr2Al steel is an important option for material selection in the injection tube of Carbon capture, utilization and storage (CCUS). X65 steel can be used for transporting CO_2 on ground with less water content.

Author contributions

Rongdie Zhu: investigation, formal analysis, validation, visualization, writing – original draft, methodology, software. Jinyang Zhu: conceptualization, data curation, funding acquisition, methodology, project administration, resources, supervision, writing – review & editing, investigation, validation. Hangrui Shi: investigation, software. Lining Xu: conceptualization, methodology, software, supervision. Yunan Zhang: conceptualization, methodology, supervision. Zhile Yang: methodology, software, validation. Yuanliang Liu: investigation, software. Hangqi Li: investigation, software.

Conflicts of interest

The authors declare that they have no known competing financial interests or personal relationships that could have appeared to influence the work reported in this paper.

Data availability

Data will be made available on request.

Supplementary information: specific data of the electrochemical impedance spectrum. See DOI: https://doi.org/10.1039/d5ra09269h.

Acknowledgements

This work is financially supported by the National Natural Science Foundation of China (52101071).

References

1 I. Czernichowski-Lauriol, R. Berenblyum, S. Bigi, M. Car, M. Gastine, S. Persoglia, N. Poulsen, C. Schmidt-Hattenberger, R. Stead, C. J. Vincent and T. Wildenborg, CO_2GeoNet actions in Europe for advancing CCUS through global cooperation, *Energy Procedia*, 2018, **154**, 73–79.

2 F. Ayello, K. Evans, N. Sridhar and R. Thodla, Effect of Liquid Impurities on Corrosion of Carbon Steel in Supercritical CO_2, *International Pipeline Conference*, 2010, pp. 111–123.

3 Y.-S. Choi, S. Nesic and D. Young, Effect of Impurities on the Corrosion Behavior of CO_2 Transmission Pipeline Steel in Supercritical CO_2^- Water Environments, *Environ. Sci. Technol.*, 2010, **44**, 9233–9238.

4 S. Sim, I. S. Cole, F. Bocher, P. Corrigan, R. P. Gamage, N. Ukwattage and N. Birbilis, Investigating the effect of salt and acid impurities in supercritical CO_2 as relevant to the corrosion of carbon capture and storage pipelines, *Int. J. Greenhouse Gas Control*, 2013, **17**, 534–541.

5 A. Pfennig and A. Kranzmann, Effect of CO_2 and pressure on the stability of steels with different amounts of chromium in saline water, *Corros. Sci.*, 2012, **65**, 441–452.

6 L. Wei, Y. Zhang, X. Pang and K. Gao, Corrosion behaviors of steels under supercritical CO_2 conditions, *Corros. Rev.*, 2015, **33**, 151–174.

7 Y. Xiang, M. Xu and Y. S. Choi, State-of-the-art overview of pipeline steel corrosion in impure dense CO_2 for CCS transportation: mechanisms and models, *Corros. Eng., Sci. Technol.*, 2017, **52**, 485–509.

8 I. S. Cole, D. A. Paterson, P. Corrigan, S. Sim and N. Birbilis, State of the aqueous phase in liquid and supercritical CO_2 as relevant to CCS pipelines, *Int. J. Greenhouse Gas Control*, 2012, **7**, 82–88.

9 J. Sun, C. Sun and Y. Wang, Effects of O_2 and SO_2 on Water Chemistry Characteristics and Corrosion Behavior of X70 Pipeline Steel in Supercritical CO_2 Transport System, *Ind. Eng. Chem. Res.*, 2018, **57**, 2365–2375.

10 Y.-S. Choi and S. Nešic, Effect Of Water Content On The Corrosion Behavior Of Carbon Steel In Supercritical CO_2 Phase With Impurities, *Corrosion*, 2011, **2011**, 11377.

11 ISO, in *Carbon dioxide capture, transportation and geological storage — Pipeline transportation systems* Switzerland, 2024.

12 E. de Visser, C. Hendriks, M. Barrio, M. J. Mølnvik, G. de Koeijer, S. Liljemark and Y. Le Gallo, Dynamis CO_2 quality recommendations, *Int. J. Greenhouse Gas Control*, 2008, **2**, 478–484.

13 Y. Hua, R. Barker and A. Neville, The influence of SO_2 on the tolerable water content to avoid pipeline corrosion during the transportation of supercritical CO_2, *Int. J. Greenhouse Gas Control*, 2015, **37**, 412–423.

14 M. Xu, Q. Zhang, X. Yang, Z. Wang, J. Liu and Z. Li, Impact of surface roughness and humidity on X70 steel corrosion in supercritical CO_2 mixture with SO_2, H_2O, and O_2, *J. Supercrit. Fluids*, 2016, **107**, 286–297.

15 A. Dugstad, M. Halseid and B. Morland, Effect of SO_2 and NO_2 on Corrosion and Solid Formation in Dense Phase CO_2 Pipelines, *Energy Procedia*, 2013, **37**, 2877–2887.

16 K. Li and Y. Zeng, Long-term corrosion and stress corrosion cracking of X65 steel in H_2O-saturated supercritical CO_2 with SO_2 and O_2 impurities, *Constr. Build. Mater.*, 2023, **362**, 129746.

17 A. Dugstad, M. Halseid, B. Morland and A. O. Sivertsen, Dense Phase CO_2 Corrosion and the Impact of

Depressurization and Accumulation of Impurities, *Corrosion*, 2013, 2785.

18 Y. Zeng, X. Pang, C. Shi, M. Arafin, R. Zavadil and J. Collier, Influence of Impurities on Corrosion Performance of Pipeline Steels in Supercritical Carbon Dioxide, *Corrosion*, 2015, 5755.

19 Y.-S. Choi, Effect of impurities on the corrosion behavior of carbon steel in supercritical CO_2-Water environments, *Corrosion*, 2010, 1–15.

20 Y. Xiang, C. Song, C. Li, E. Yao and W. Yan, Characterization of 13Cr steel corrosion in simulated EOR-CCUS environment with flue gas impurities, *Process Saf. Environ. Prot.*, 2020, **140**, 124–136.

21 Y. Wang, B. Wang, S. He, L. Zhang, X. Xing, H. Li and M. Lu, Unraveling the effect of H_2S on the corrosion behavior of high strength sulfur-resistant steel in $CO_2/H_2S/Cl^-$ environments at ultra high temperature and high pressure, *J. Nat. Gas Sci. Eng.*, 2022, **100**, 104477.

22 D. S. Carvalho, C. J. B. Joia and O. R. Mattos, Corrosion rate of iron and iron–chromium alloys in CO_2 medium, *Corros. Sci.*, 2005, **47**, 2974–2986.

23 B. Kermani, J. C. Gonzales, G. L. Turconi, L. Pigliacampo, T. Perez and C. Morales, Window of Application and Operational Track Record of Low Carbon 3Cr Steel Tubular, *Corrosion*, 2006, 1–14.

24 J. Zhu, L. Xu, M. Lu, L. Zhang, W. Chang and L. Hu, Essential criterion for evaluating the corrosion resistance of 3Cr steel in CO_2 environments: Prepassivation, *Corros. Sci.*, 2015, **93**, 336–340.

25 F. Liu, H. Li, Y. Zhang, R. Zhu and J. Zhu, Complete inhibition of localized corrosion in 5Cr steel under a water-saturated supercritical CO_2 environment through Al microalloying, *RSC Adv.*, 2025, **15**, 7876–7884.

26 F. Liu, Y. Zhang and J. Zhu, Effect of Al content on corrosion performance of Fe-5Cr-xAl steels in supercritical CO_2-saturated brine environments, *Electrochim. Acta*, 2025, **540**, 147208.

27 R. Zhu, J. Zhu, Y. Zhang and Z. Yang, Effects of SO_2 impurity on corrosion behaviors of novel 3Cr2Al alloy steel in supercritical CO_2 brine environment, *Corros. Sci.*, 2025, **255**, 113109.

28 Y.-S. Choi, S. Hassani, T. N. Vu, S. Nešić and A. Z. B. Abas, Effect of H_2S on the Corrosion Behavior of Pipeline Steels in Supercritical and Liquid CO_2 Environments, *Corrosion*, 2016, **72**, 999–1009.

29 Y. Zhang, X. Pang, S. Qu, X. Li and K. Gao, Discussion of the CO_2 corrosion mechanism between low partial pressure and supercritical condition, *Corros. Sci.*, 2012, **59**, 186–197.

30 G. A. Zhang, D. Liu, Y. Z. Li and X. P. Guo, Corrosion behaviour of N80 carbon steel in formation water under dynamic supercritical CO_2 condition, *Corros. Sci.*, 2017, **120**, 107–120.

31 Y. Hua, S. Mohammed, R. Barker and A. Neville, Comparisons of corrosion behaviour for X65 and low Cr steels in high pressure CO_2-saturated brine, *J. Mater. Sci. Technol.*, 2020, 21–32.

32 Y. Zhang, K. Gao and G. Schmitt, Water effect on steel under supercritical CO_2 condition, *Int. Corros. Conf. Ser.*, 2011, 1–15.

33 X. Yue, L. Zhang, L. Ma, M. Lu, A. Neville and Y. Hua, Influence of a small velocity variation on the evolution of the corrosion products and corrosion behaviour of super 13Cr SS in a geothermal CO_2 containing environment, *Corros. Sci.*, 2021, **178**, 108983.

34 L. Wei, X. Pang, C. Liu and K. Gao, Formation mechanism and protective property of corrosion product scale on X70 steel under supercritical CO_2 environment, *Corros. Sci.*, 2015, **100**, 404–420.

35 S. Guo, L. Xu, L. Zhang, W. Chang and M. Lu, Characterization of corrosion scale formed on 3Cr steel in CO_2-saturated formation water, *Corros. Sci.*, 2016, **110**, 123–133.

36 J. Chastain and R. C. King Jr, *Handbook of X-Ray Photoelectron Spectroscopy*, Perkin-Elmer Corporation, 1992, vol. 40, p. 25.

37 W. Sun, S. Nešic and S. Papavinasam, Kinetics of corrosion layer formation. Part 2—Iron sulfide and mixed iron sulfide/carbonate layers in carbon dioxide/hydrogen sulfide corrosion, *Corrosion*, 2008, **64**, 586–599.

38 S. Guo, L. Xu, L. Zhang, W. Chang and M. Lu, Corrosion of alloy steels containing 2% chromium in CO2 environments, *Corros. Sci.*, 2012, **63**, 246–258.

39 Y. Tang, X. Guo and G. Zhang, Corrosion behaviour of X65 carbon steel in supercritical-CO2 containing H2O and O2 in carbon capture and storage (CCS) technology, *Corros. Sci.*, 2017, **118**, 118–128.

40 F. Berger, E. Beche, R. Berjoan, D. Klein and A. Chambaudet, An XPS and FTIR study of SO2 adsorption on SnO2 surfaces, *Appl. Surf. Sci.*, 1996, **93**, 9–16.

41 T. Song, *X-Ray Photoelectron Spectroscopy Data Analysis*, Beijing Institute of Technology Press Co., Ltd., 2022.

42 E. Desimoni, C. Malitesta, P. Zambonin and J. Riviere, An X-ray photoelectron spectroscopic study of some chromium–oxygen systems, *Surf. Interface Anal.*, 1988, **13**, 173–179.

43 T. Moffat, R. Latanision and R. Ruf, An X-ray photoelectron spectroscopy study of chromium-metalloid alloys—III, *Electrochim. Acta*, 1995, **40**, 1723–1734.

44 G. A. Zhang, M. X. Lu, Y. B. Qiu, X. P. Guo and Z. Y. Chen, The Relationship between the Formation Process of Corrosion Scales and the Electrochemical Mechanism of Carbon Steel in High Pressure CO_2-Containing Formation Water, *J. Electrochem. Soc.*, 2012, **159**, C393.

45 J. Zhang, Z. L. Wang, Z. M. Wang and X. Han, Chemical analysis of the initial corrosion layer on pipeline steels in simulated CO_2-enhanced oil recovery brines, *Corros. Sci.*, 2012, **65**, 397–404.

46 F. Farelas, M. Galicia, B. Brown, S. Nesic and H. Castaneda, Evolution of dissolution processes at the interface of carbon steel corroding in a CO_2 environment studied by EIS, *Corros. Sci.*, 2010, **52**, 509–517.

47 T. Hemmingsen, H. Vangdal and T. Våland, Formation of Ferrous Sulfide Film from Sulfite on Steel Under Anaerobic Conditions, *Corrosion*, 1992, **48**, 475–481.

48 T. Hemmingsen and T. Vland, The reaction of the sulphite/bisulphite couple on SMO steel under anaerobic conditions, *Electrochim. Acta*, 1991, **36**, 1367–1375.
49 C. Pan, W. Wang, A. K. Horváth, J. Xie, Y. Lu, Z. Wang, C. Ji and Q. Gao, Kinetics and Mechanism of Alkaline Decomposition of the Pentathionate Ion by the Simultaneous Tracking of Different Sulfur Species by High-Performance Liquid Chromatography, *Inorg. Chem.*, 2011, **50**, 9670–9677.
50 C. Ren, D. Liu, Z. Bai and T. Li, Corrosion behavior of oil tube steel in simulant solution with hydrogen sulfide and carbon dioxide, *Mater. Chem. Phys.*, 2005, **93**, 305–309.
51 Y. Tang, X. P. Guo and G. A. Zhang, Corrosion behaviour of X65 carbon steel in supercritical-CO_2 containing H_2O and O_2 in carbon capture and storage (CCS) technology, *Corros. Sci.*, 2017, **118**, 118–128.
52 I. S. Cole, P. Corrigan, S. Sim and N. Birbilis, Corrosion of pipelines used for CO_2 transport in CCS: is it a real problem?, *Int. J. Greenhouse Gas Control*, 2011, **5**, 749–756.
53 G. A. Zhang and Y. F. Cheng, On the fundamentals of electrochemical corrosion of X65 steel in CO_2-containing formation water in the presence of acetic acid in petroleum production, *Corros. Sci.*, 2009, **51**, 87–94.
54 L. Xu, J. Zhu and B. Wang, Influence of Cr content and PH value on the semi-passivation behavior of low Cr pipeline steels, *Acta Metall. Sin.*, 2017, **53**, 677–683.
55 H. Ding, Y. Xiang, Y. Zhang, Z. Yang, Z. Zhao, K. Yan, C. Li, W. Zhang, Y. Zhao and R. Jia, A mechanistic corrosion prediction model for the casing system of sequestration wells in supercritical CO_2-saturated aqueous environment with multi-impurities, *Corros. Sci.*, 2025, **256**, 113203.